# Numerical Simulation of Supersonic Flow Over a Three-Dimensional Cavity

Donald P. Rizzetta*
*U.S. Air Force Wright Aeronautical Laboratories, Wright-Patterson Air Force Base, Ohio*

**A numerical solution is presented for the unsteady flow over a three-dimensional cavity at a freestream Mach number of 1.5 and Reynolds number of $1.09 \times 10^6$. The self-sustained oscillatory motion within the cavity is generated numerically by integration of the time-dependent compressible three-dimensional Reynolds averaged Navier-Stokes equations. Effects of fine-scale turbulence are simulated via a simple algebraic closure model. Details of the flowfield structure are elucidated, and it is verified that the fundamental behavior of the unsteady phenomena is two dimensional. Comparison with experimental data is made in terms of the mean static pressure and overall acoustic sound pressure levels within the cavity, as well as with the acoustic frequency spectra of the oscillation along the cavity floor and rear bulkhead.**

## Nomenclature

$c$ = local speed of sound, $(\gamma RT)^{1/2}$
$C_p$ = mean static pressure coefficient, $2(\bar{p} - p_\infty)/\rho_\infty u_\infty^2$
$D$ = cavity depth
$e$ = internal specific energy
$E$ = total specific energy
$F,G,H$ = vector fluxes
$L$ = cavity length
$M$ = Mach number
$n$ = normal direction
$p$ = static pressure
$\bar{p}$ = mean static pressure, $\dfrac{1}{(t_f - t_i)} \displaystyle\int_{t_i}^{t_f} p \, dt$
$\overline{p'^2}$ = mean squared fluctuating pressure, $\dfrac{1}{(t_f - t_i)} \displaystyle\int_{t_i}^{t_f} (p - \bar{p})^2 dt$
$Pr$ = Prandtl number, 0.73 for air
$Pr_t$ = turbulent Prandtl number, 0.9
$q$ = acoustic sound reference level, $2 \times 10^{-5}$ *Pa*
$q_x,q_y,q_z$ = components of heat flux vector
$R$ = gas constant
$SPL$ = sound pressure level, $10 \log_{10}\left[\dfrac{\overline{p'^2}}{q^2}\right]$
$t$ = time
$T$ = temperature
$u,v,w$ = Cartesian velocity components in $x,y,z$ directions
$u_{1,2,3}$ = $u,v,w$
$U$ = vector of dependent mass-averaged variables
$W$ = cavity width
$x,y,z$ = Cartesian coordinates in streamwise, normal, and spanwise directions
$y^+$ = law-of-the-wall coordinate, $\left(\dfrac{\rho}{\mu}\dfrac{\partial u}{\partial y}\right)_w^{1/2} y$
$\beta$ = pressure damping coefficient
$\gamma$ = specific heat ratio, 1.4 for air
$\delta$ = boundary-layer thickness
$\Delta$ = finite-difference step size
$\theta$ = characteristic Mach wave angle, $\arcsin(1/M)$
$\mu$, $u_t$ = molecular and turbulent viscosity coefficients, respectively
$\nu_{1,2,3}$ = $\xi,\eta,\zeta$
$\xi,\eta,\zeta$ = transformed coordinates
$\rho$ = fluid density
$\tau_{xx},\tau_{yy},\tau_{zz}$
$\tau_{xy},\tau_{xz},\tau_{yz}$ = components of stress tensor

*Subscripts*

$aw$ = adiabatic wall value
$f$ = final value
$i$ = initial value
$min$ = minimum value
$s$ = standard value
$u$ = evaluated at upstream corner
$w$ = wall value
$\infty$ = freestream value

## Introduction

HIGH speed flows over open cavities produce complex unsteady flowfields that are of fundamental physical interest and pose a significant practical concern in aerospace applications. At high Reynolds numbers, such flows are characterized by a severe acoustic environment within the cavity, which consists of both "broadband" small-scale pressure fluctuations typical of turbulent shear layers, as well as discrete resonance whose frequency, amplitude, and harmonic properties depend upon the cavity geometry and external flow conditions. These phenomena represent a potential hazard to structural members in proximity to the cavity, may adversely affect aerodynamic performance or stability, and can damage sensitive instrumentation.

Numerous prior investigations[1-15] have been conducted in order to gain insight into the underlying physical behavior of cavity flows. While most of these have been experimental, simplified analytic analyses and empirical techniques have made it possible to predict some of the features of observed phenomena. More recently, numerical solutions of the governing fluid

Received March 2, 1987; presented as Paper 87-1288 at the AIAA 19th Fluid Dynamics, Plasma Dynamics and Lasers Conference, Honolulu, HI, June 8-10, 1987; revision received Sept. 24, 1987. 

*Aerospace Engineer. Associate Fellow AIAA.

equations of motion[12,13] have provided a detailed flowfield description that was not obtainable by previous methods.

All of these studies have contributed to an understanding of the flow-induced oscillations produced by a supersonic stream flowing over an open rectangular cavity. Such oscillations are commonly attributed to the interaction between the free shear layer, lying above the cavity mouth, and the external stream, which results in periodic addition and removal of mass near the aft bulkhead. This process is depicted schematically in Fig. 1 and is briefly reviewed here for clarity.

Figure 1a indicates a pressure wave propagating downstream and approaching the aft bulkhead. This wave produces an outward deflection of the shear layer that allows fluid to leave the cavity at the aft end. Upstream, a pressure wave, which previously had been traveling upstream, is reflected from the forward bulkhead and now also moves downstream. In Fig. 1b, the upstream wave continues to travel downstream. The downstream wave, however, has reflected from the aft bulkhead and propagates upstream through the relatively quiescent fluid within the cavity. Because this wave moves supersonically with respect to the freestream, a compression wave is generated in the external flow. At the rear bulkhead, the shear layer lies below the cavity lip, resulting in mass addition to the interior region. The forward and rearward propagating waves intersect near the center of the cavity and, after interacting, maintain their respective directions of motion as shown in Fig. 1c. At the aft bulkhead, the shear layer continues to inject fluid into the cavity, thus creating a recirculating flow. In Fig. 1d, the aft wave is seen to lift the shear layer above the downstream lip, resulting in mass removal, while the forward wave is about to impact the upstream bulkhead and complete the oscillation cycle which began with the situation depicted initially in Fig. 1a.

This simplified explanation of cavity oscillation has made it possible to eliminate large amplitude unsteady motion in aircraft wheel wells and weapon bays where such fluctuations can produce damaging effects. By modifying the aft bulkhead to form a ramp at the downstream end of the cavity, the huge addition and removal of mass, due to the shear layer alternately attaching and separating from the rear vertical surface, may be alleviated. More commonly employed is a fence along the upstream lip of the cavity that produces massive separation and thus precludes shear-layer oscillation.

An alternative model, which is not inconsistent with the description depicted in Fig. 1, was suggested by Rossiter.[5] He proposed a feedback loop whereby the shear layer was considered to consist of a series of vortices that originate at the upstream cavity lip and travel downstream at a constant velocity. Upon reaching the downstream lip, the vortices immediately produce upstream propagating acoustic waves that move at the local speed of sound. When these waves impact the upstream lip, they trigger the production of new vortices, thereby completing the feedback loop. From this simple concept an empirical relationship was then constructed in order to predict the oscillation frequencies of the cavity. Rossiter also points out that even for three-dimensional cavities the fundamental behavior, particularly along the centerline, appears to be predominantely two-dimensional.

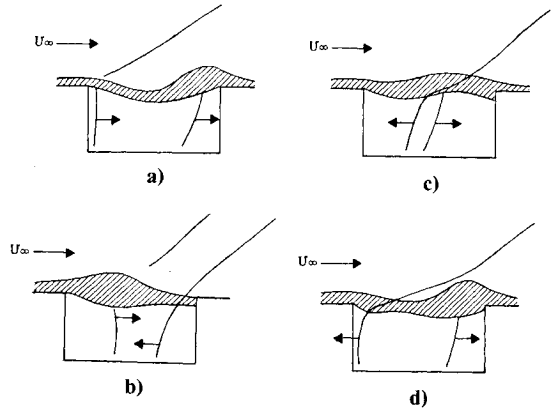


Fig. 1 Schematic representation of cavity oscillation.

It should be noted that in order for the oscillation to be self-sustaining, an amplification of disturbances must occur within the feedback loop. Without such amplification, the oscillation would eventually terminate due to dissipation. In this regard, a simple linearized shear layer stability analysis has been employed for investigating the amplification.[13]

While the oscillation frequencies for cavity flows may be predicted by empirical formulas, no simple analytic analysis will yield the associated amplitude of the fluctuating pressure. Numerical solution of the governing fluid equations of motion, however, can provide this and other detailed information describing the flowfield structure. The first such calculation was produced by Borland[12] who solved the two-dimensional Euler equations for the high subsonic flow over a cavity having a length to depth ratio of 2.0. Subsequently, Hankey and Shang[13] computed the flow over a cavity with a length to depth ratio of 2.25 at a freestream Mach number of 1.5 by numerically integrating the two-dimensional Navier-Stokes equations. This calculation made no attempt to account for small-scale turbulence, even though the Reynolds number was quite high. The solution agreed quite well with experimental data in terms of mean static pressure and the amplitude of the oscillation, although it was not possible to resolve the harmonic frequencies accurately.

With the current capacity of large-scale computing machinery, it is now possible to perform extensive calculations of cavity flows that need not be limited to two-dimensional simulations or approximate sets of equations. Complex geometric configurations, including bay doors, landing gear, stores, and release mechanisms, may be considered. While such calculations are possible, little experience is available for judging either their quality or adequacy as predictive tools. It is the purpose of the present computation to help provide such information.

The configuration to be considered and the associated coordinate system is represented schematically in Fig. 2. This cavity has a length to depth ratio ($L/D$) of 5.07, a length to width ratio ($L/W$) of 1.90, and represents one of the cases of the comprehensive experimental data of Kaufman et al.[15] Because the configuration is symmetric about the cavity centerline, a half-span computational model was employed so that the three-dimensional flowfield could be more fully resolved. The freestream Mach number of 1.5 and the Reynolds number of $1.09 \times 10^6$, based on freestream conditions and the cavity length, duplicate the test conditions of the experiment.

## Governing Equations

The governing equations are taken to be the unsteady compressible three-dimensional Navier-Stokes equations written in mass-averaged variables which in the absence of external forces may be expressed notationally in the following chain-rule con-

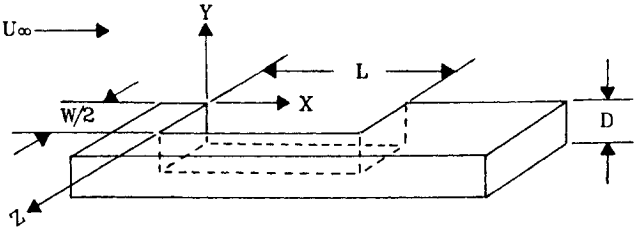


Fig. 2 Cavity geometry.

servative form:

$$\frac{\partial U}{\partial t}+\left[\frac{\partial \xi}{\partial x},\frac{\partial \xi}{\partial y},\frac{\partial \xi}{\partial z}\right]\begin{bmatrix}\frac{\partial F}{\partial \xi}\\ \frac{\partial G}{\partial \xi}\\ \frac{\partial H}{\partial \xi}\end{bmatrix}+\left[\frac{\partial \eta}{\partial x},\frac{\partial \eta}{\partial y},\frac{\partial \eta}{\partial z}\right]\begin{bmatrix}\frac{\partial F}{\partial \eta}\\ \frac{\partial G}{\partial \eta}\\ \frac{\partial H}{\partial \eta}\end{bmatrix}+\left[\frac{\partial \zeta}{\partial x},\frac{\partial \zeta}{\partial y},\frac{\partial \zeta}{\partial z}\right]\begin{bmatrix}\frac{\partial F}{\partial \zeta}\\ \frac{\partial G}{\partial \zeta}\\ \frac{\partial H}{\partial \zeta}\end{bmatrix}=0 \tag{1}$$

Here $x$, $y$, $z$ are Cartesian coordinates in the streamwise, normal, and spanwise directions, respectively (see Fig. 2), $\xi,\eta,\zeta$ the corresponding coordinates in the computational system, and

$$U=\begin{bmatrix}\rho\\ \rho u\\ \rho v\\ \rho w\\ \rho E\end{bmatrix} \tag{2}$$

$$F=\begin{bmatrix}\rho u\\ \rho u^2+\tau_{xx}\\ \rho uv+\tau_{xy}\\ \rho uw+\tau_{xz}\\ (\rho E+\tau_{xx})u+\tau_{xy}v+\tau_{xz}w-q_x\end{bmatrix} \tag{3}$$

$$G=\begin{bmatrix}\rho v\\ \rho vu+\tau_{yx}\\ \rho v^2+\tau_{yy}\\ \rho vw+\tau_{yz}\\ (\rho E+\tau_{yy})v+\tau_{yx}u+\tau_{yz}w-q_y\end{bmatrix} \tag{4}$$

$$H=\begin{bmatrix}\rho w\\ \rho wu+\tau_{zx}\\ \rho wv+\tau_{zy}\\ \rho w^2+\tau_{zz}\\ (\rho E+\tau_{zz})w+\tau_{zx}u+\tau_{zy}v-q_z\end{bmatrix} \tag{5}$$

$$\tau_{xx}=p+\frac{2}{3}(\mu+\mu_t)\left(\frac{\partial u}{\partial x}+\frac{\partial v}{\partial y}+\frac{\partial w}{\partial z}\right)-2(\mu+\mu_t)\frac{\partial u}{\partial x} \tag{6a}$$

$$\tau_{yy}=p+\frac{2}{3}(\mu+\mu_t)\left(\frac{\partial u}{\partial x}+\frac{\partial v}{\partial y}+\frac{\partial w}{\partial z}\right)-2(\mu+\mu_t)\frac{\partial v}{\partial y} \tag{6b}$$

$$\tau_{zz}=p+\frac{2}{3}(\mu+\mu_t)\left(\frac{\partial u}{\partial x}+\frac{\partial v}{\partial y}+\frac{\partial w}{\partial z}\right)-2(\mu+\mu_t)\frac{\partial w}{\partial z} \tag{6c}$$

$$\tau_{xy}=\tau_{yx}=-(\mu+\mu_t)\left(\frac{\partial u}{\partial y}+\frac{\partial v}{\partial x}\right) \tag{7a}$$

$$\tau_{xz}=\tau_{zx}=-(\mu+\mu_t)\left(\frac{\partial u}{\partial z}+\frac{\partial w}{\partial x}\right) \tag{7b}$$

$$\tau_{yz}=\tau_{zy}=-(\mu+\mu_t)\left(\frac{\partial v}{\partial z}+\frac{\partial w}{\partial y}\right) \tag{7c}$$

$$q_x=\gamma\left(\frac{\mu}{Pr}+\frac{\mu_t}{Pr_t}\right)\frac{\partial e}{\partial x} \tag{8a}$$

$$q_y=\gamma\left(\frac{\mu}{Pr}+\frac{\mu_t}{Pr_t}\right)\frac{\partial e}{\partial y} \tag{8b}$$

$$q_z=\gamma\left(\frac{\mu}{Pr}+\frac{\mu_t}{Pr_t}\right)\frac{\partial e}{\partial z} \tag{8c}$$

$$E=e+(u^2+v^2+w^2)/2 \tag{9}$$

In the preceding expressions $u$, $v$, and $w$ are the Cartesian velocity components, $\rho$ is the density, $p$ the pressure, and $e$ the specific internal energy. The Sutherland Law for the laminar viscosity coefficient $\mu$ and the perfect gas relationship

$$p=\rho RT \tag{10}$$

are also employed. Effects of fine-scale turbulence are accounted for by specifying a turbulent Prandtl number $Pr_t=0.9$, and incorporating a simple algebraic closure model for the turbulent viscosity coefficient, $\mu_t$. For this purpose, the two-layer formulation of Baldwin and Lomax,[16] with minor modification, is used. At all grid points lying directly above the planar surface surrounding the mouth of the cavity, the Baldwin-Lomax model is applied intact. For those points above the floor of the cavity, $\mu_t$ is calculated according to the following expression

$$\mu_t=\mu_{tu}+(\mu_{ts}-\mu_{tu})[1-\exp(-x/10\delta)] \tag{11}$$

Here $\mu_{ts}$ is the unaltered Baldwin-Lomax value, $\mu_{tu}$ the value at the upstream corner ($x=0$), and $\delta$ the instantaneous boundary-layer thickness at the upstream corner. Note that $\mu_{tu}$, $\mu_{ts}$, and $\delta$ are all evaluated at the same spanwise location and that $x$ is the streamwise distance from the corner. It was deemed that this relaxation model, which has been shown to work well for other numerical calculations,[17] would allow the eddy-viscosity model to account for history effects of the fluid. The coefficient is set to zero along all solid surfaces interior to the cavity, and no special provision is made to modify the model length scale near the intersection of planar surfaces.

On all solid boundaries, the no-slip conditions

$$u=v=w=0 \tag{12}$$

were invoked, along with

$$\frac{\partial p}{\partial n}=0 \tag{13}$$

$$T=T_{aw} \tag{14}$$

where $n$ is the direction normal to the rigid surface. The isothermal wall temperature, $T_{aw}$, was taken as the adiabatic wall value of 542.7°R which compares well with the measured temperatures[15] of 539° and 545°R at two wall locations. For sharp corners formed by the intersection of planar cavity walls, the pressure was determined by extrapolating along each wall to the corner and averaging the result. At such locations, this treatment was employed in lieu of Eq. 13, thereby circumventing any ambiguity regarding the normal direction. Upstream boundary conditions were obtained from the numerical solution of the two-dimensional equations of motion for steady flow over a flat plate at the freestream conditions of the cavity flow. This calculation employed the same normal grid distribution as was used for the cavity computation, so that interpolation could be avoided. The flat plate computational domain extended from the leading edge of the cavity experimental configuration ($x=-1.532L$) to the forward bulkhead using a uniform streamwise mesh spacing of $\Delta x=0.015L$ and 101 $x$-grid locations. Results of this solution at $x=-0.19842L$ then established upstream profiles of the dependent variables, including $\mu_t$, at all spanwise stations.

Downstream boundary conditions were obtained by simple zeroth-order extrapolation from the interior domain, corresponding to the condition

$$\frac{\partial U}{\partial \xi}=0 \tag{15}$$

Along the centerline, the symmetry conditions

$$\frac{\partial \rho}{\partial \zeta} = \frac{\partial (\rho u)}{\partial \zeta} = \frac{\partial (\rho v)}{\partial \zeta} = \frac{\partial (\rho E)}{\partial \zeta} = w = 0 \tag{16}$$

were imposed, while at the outboard boundary, spanwise derivatives were forced to vanish, i.e.

$$\frac{\partial U}{\partial \zeta} = 0 \tag{17}$$

At the upper computational boundary, derivatives along instantaneous Mach lines were set to zero, which had previously proven successful in the two-dimensional case.[13] Neglecting spanwise variations, this condition was expressed as

$$(\xi_x + \xi_y \tan\theta)\frac{\partial U}{\partial \xi} + (\eta_x + \eta_y \tan\theta)\frac{\partial U}{\partial \eta} = 0 \tag{18}$$

where

$$\theta = \arcsin(1/M) \tag{19}$$

Initial conditions were taken as the flat plate profile at all grid locations lying above the cavity mouth. For the interior points, wall values were assigned.

## Numerical Procedure

The geometric configuration to be considered consisted of the half-span model represented schematically in Fig. 2 with the following dimensions: $L = 0.12065m$, $D = 0.02381m$, and $W = 0.06350m$. The surrounding computational domain was described by a nonuniform Cartesian mesh whose grid lines at the upstream and inboard boundaries are shown in Fig. 3 and consisted of $105 \times 35 \times 30$ points on and above the plane of the mouth and $75 \times 29 \times 20$ points inside the cavity, in the $x,y,z$ directions, respectively. This distribution employed 11 $x$-grid points at an upstream of the forward bulkhead and 20 at or downstream of the aft bulkhead. Overall extent of the domain was $-0.19842 \le x/L \le 1.5$, $0 \le y/D \le 5.05333$, and $0 \le z/W \le 0.94546$. As shown in the figure, clustering of grid lines was employed at the forward and aft bulkheads, at the plane of the mouth, and at the sidewall. For this purpose, simple exponential stretching was used, with the following minimum grid spacings: $\Delta x_{min}/L = \Delta z_{min}/L = 0.00505263$ and $\Delta y_{min}/L = 0.00202105$.

Within the cavity, the $y$ coordinate was stretched from the minimum value at the plane of the mouth to a constant value of $\Delta y/L = 0.00902$, which occurred over the first 15 $y$-grid lines. At the plane of symmetry, the first 11 $z$-grid lines had the uniform spacing of $\Delta z/L = 0.01784$. The distributions were constructed in order to provide adequate resolution of the flow inside the cavity itself. At the upstream computational boundary, the normal spacing resulted in a value of $y^+ = 4.43$ at the first $y$ mesh point above the plane of the mouth, as computed from the turbulent flat-plate profile. This profile also consisted of approximately 15 points within the boundary layer and was deemed to be adequate for the shear layer which grows in normal extent downstream. Metric coefficients of the transformation from the physical domain $(x,y,z)$ shown in Fig. 3 to the uniformly distributed computational system $(\xi,\eta,\zeta)$, appear in Eq. 1 and were evaluated numerically by second-order-accurate formulas corresponding to central differences at interior mesh points and one-sided differences at solid surfaces and computational boundaries.

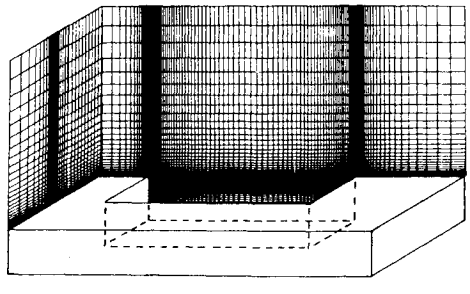

Fig. 3 Computational grid.

Unsteady solutions to Eq. 1 were obtained using the time-dependent, explicit, unsplit two-step predictor-corrector finite-difference algorithm of MacCormack,[18] which has evolved as a reliable technique for obtaining numerical solutions to a wide variety of complex fluid flow problems. This two-step process consists of evaluating spatial derivatives by one-sided differences taken in opposite directions on alternate steps. In order to resolve the high-frequency content of the unsteady flowfield, the direction of these differences was cyclically permuted, thus maintaining true second-order temporal accuracy. As part of the algorithm, a fourth-order pressure damping term,[19] commonly employed to suppress numerical oscillations arising from regions with large gradients in the dependent variables, was incorporated. Damping was implemented in the form

$$\beta \Delta\tau \sum_{i=1}^{3} \Delta v_i^3 \frac{\partial}{\partial v_i}\left[\frac{\partial U}{\partial v_i}\left|\frac{\partial^2 p}{\partial v_i^2}\right|\frac{|u_i + c|}{p}\right] \tag{20}$$

where $v_{1,2,3} = \xi,\eta,\zeta$, $u_{1,2,3} = u,v,w$. The damping term is added to the new value of $U$ at the completion of each predictor or corrector step. For the solutions presented here, the damping coefficient $\beta = 2.0$ was employed.

The aforementioned features of the numerical algorithm were embodied in an efficient vectorized solver written especially for the CRAY-2 computer. Owing to the explicit nature of the algorithm and the vast storage capacity of the CRAY-2, the grid system was treated as a single $105 \times 64 \times 30$ block structure. At the completion of each predictor or corrector step, solid boundaries were reset to wall values. This procedure required the additional storage of "wasted" grid points within solid surfaces but provided the enhanced efficiency of long vectors in a single-block flow solver. Moreover, the added complexity of matching the solution at interfacing blocks was avoided, and second-order temporal accuracy could easily be maintained. Approximately 4.8 million 64-bit words of central memory were required, and a mean data processing rate of $4.48 \times 10^{-5}$ CPU s/time step/grid point was achieved.

## Results

Starting from the initial profiles, the flowfield solution was integrated in time at a maximum local CFL number of 0.5, which was chosen as a conservative value for stability considerations. After 5000 time steps, corresponding to 4.27 characteristic times $(u_\infty t/L)$, it was judged that the flowfield had been purged of initial transients and the oscillation was self-sustaining. Time dependent data was collected for 32,000 time steps for comparison with experimental measurements. The total time interval over which data was gathered corresponded to 23.23 characteristic times. Processing of the entire computation required approximately 92.3 CPU hours on the CRAY-2. In addition to the three-dimensional calculation, a two-dimensional solution, employing the same $x$-$y$ grid system, was also generated. All aspects of the two computations were identical, including boundary and initial conditions, CFL number, and damping coefficient.

Results of these calculations appear in Fig. 4 in terms of the mean static streamwise pressure distributions along the cavity floor at the plane of symmetry ($y = 0$, $z = 0$) and along the sidewall at mid-depth ($y/D = 0.5$, $z/W = 0.5$). Here, the pressure coefficient $Cp$ is defined as

$$Cp = \frac{2(\bar{p} - p_\infty)}{\rho_\infty u_\infty^2} \tag{21}$$

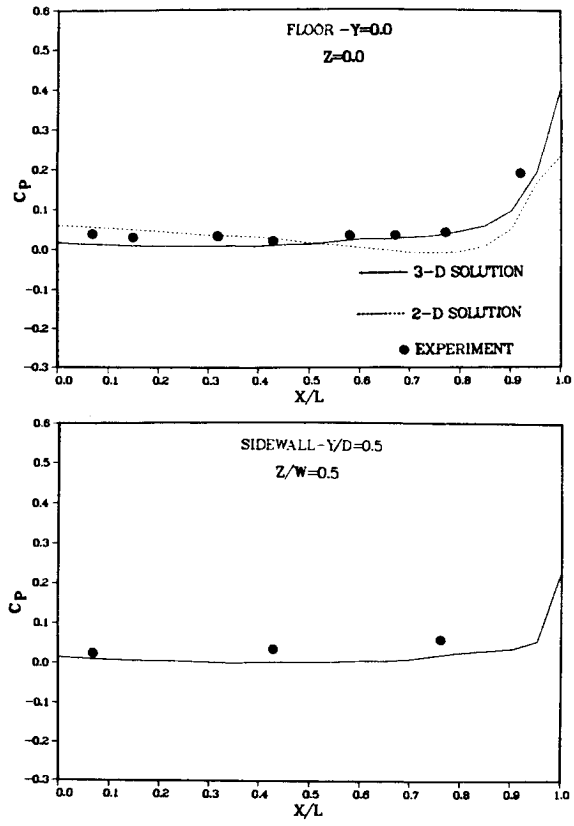


Fig. 4 Mean static pressure—streamwise distribution along the floor at the centerline and along the sidewall at $y/D = 0.5$.

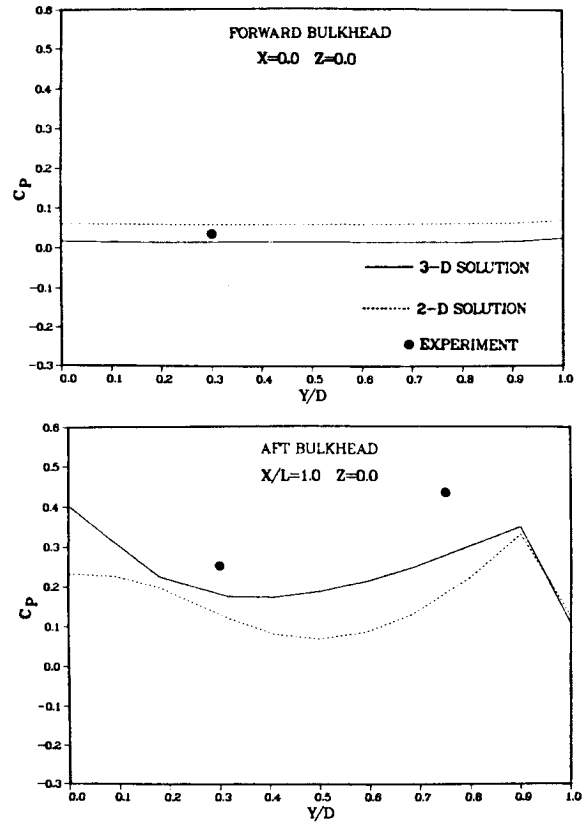


Fig. 5 Mean static pressure—normal distribution along the forward and aft bulkheads at the centerline.

where

$$\bar{p} = \left(\frac{1}{t_f - t_i}\right) \int_{t_i}^{t_f} p \, dt \tag{22}$$

The pressure distribution is seen to be relatively constant over the first 80% of the length of the cavity and then rise sharply near the aft bulkhead. Generally, the three-dimensional solution compares favorably with experiment. The two-dimensional result slightly overpredicts the pressure level upstream of midcavity and underpredicts the level downstream.

Figure 5 displays the corresponding centerline pressure distributions on the forward and aft bulkheads. At the forward bulkhead, the pressure is virtually constant, while in the aft pressure, there are local maximums at the floor ($y/D = 0$) and near the top of the cavity ($y/D = 1$) where effects of the shear layer are most pronounced. Consistent with Fig. 4, the two-dimensional result overpredicts the pressure upstream and underpredicts it downstream. Differences between the numerical solution and experimental data are notable on the rear bulkhead where the magnitude of the fluctuating pressure is the greatest and thus most sensitive to either experimental or numerical inaccuracy.

In Fig. 6, the acoustic streamwise pressure distributions along cavity floor and sidewall are represented as overall sound pressure level, *SPL*, in decibels, which is defined as

$$SPL = 10 \log_{10}\left(\frac{\overline{p'^2}}{q^2}\right) \tag{23}$$

with

$$\overline{p'^2} = \left(\frac{1}{t_f - t_i}\right) \int_{t_i}^{t_f} (p - \bar{p})^2 \, dt \tag{24}$$

and $q$ the acoustic sound reference level of $2 \times 10^{-5}$ Pa. The numerical solution appears to be within 5 dB of the experi-

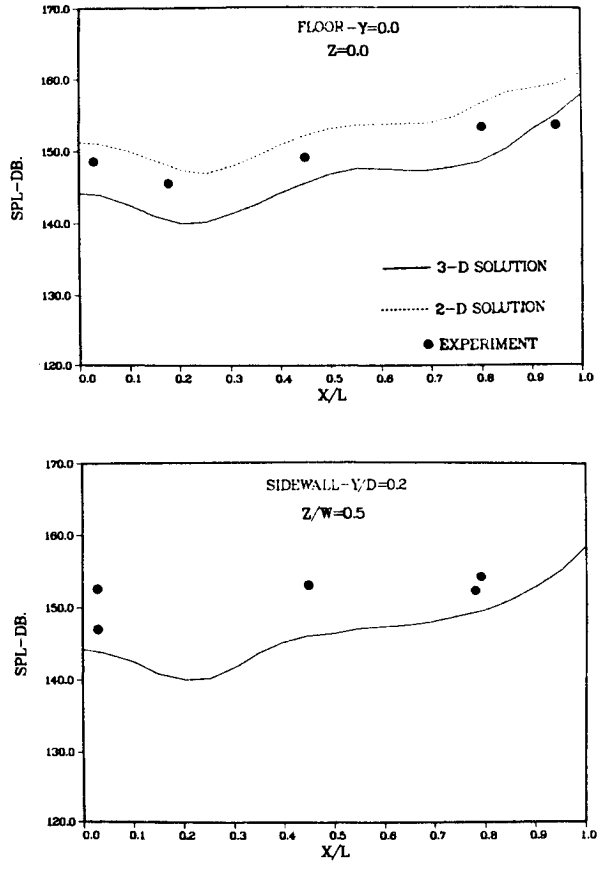


Fig. 6 Overall sound pressure level—streamwise distribution along the floor at the centerline and along the sidewall at $y/D = 0.2$.

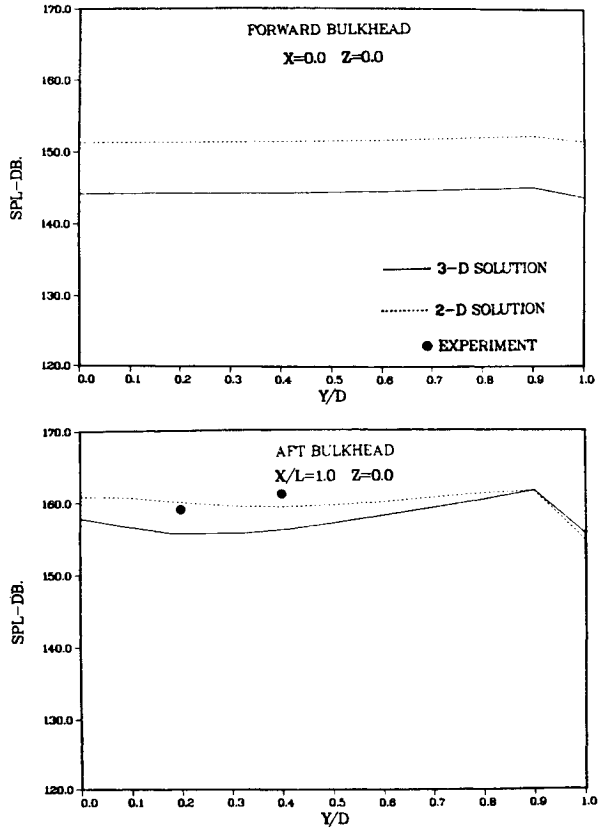


**Fig. 7 Overall sound pressure level—normal distribution along the forward and aft bulkheads at the centerline.**

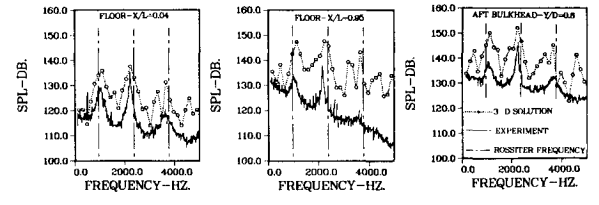


**Fig. 8 Frequency spectra of sound pressure level on floor and rear bulkhead at the centerline—comparison between numerical solution and experimental data.**

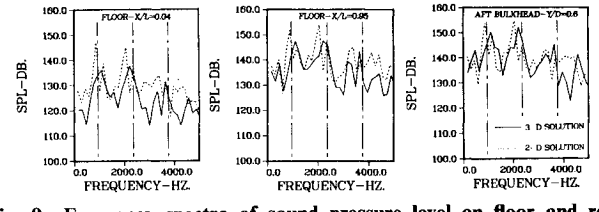


**Fig. 9 Frequency spectra of sound pressure level on floor and rear bulkhead at the centerline—comparison between two- and three-dimensional numerical solutions.**

ment. Also noted is the fact that the two-dimensional result overpredicts the level uniformly by about 8 dB, except near the rear bulkhead. These trends are also apparent in the corresponding overall sound pressure levels along the bulkheads shown in Fig. 7. As expected, the aft bulkhead experiences a 10–15 dB higher *SPL* than does the forward bulkhead.

Shown in Fig. 8 is the frequency spectra contributing to the overall sound pressure level at three positions along the cavity

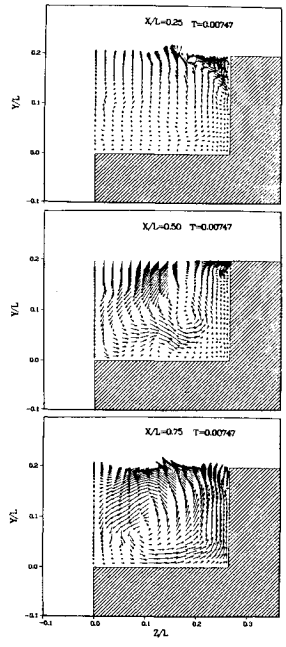


**Fig. 10 Instantaneous cross-plane velocity vectors at $t = t_f$.**

centerline where data was taken. Two of the positions are on the floor, and one is at the aft bulkhead. For comparison, the predicted oscillation frequencies obtained from Rossiter's modified equation[15] are also shown. The harmonic frequencies predicted by the computation appear to agree well with the experiment. While the amplitude level of the calculation is generally higher than the experimental result, harmonic peaks agree to within about 10 dB. It should be mentioned that the computed solution described a total sampling time of only $6.31 \times 10^{-3}$ s, thus limiting the data analysis to an incremental frequency with a bandwidth of 158.4 Hz, as can be seen in the figure. Because the experimental analysis employed an incremental bandwidth of 8 Hz, the computation was corrected to account for this disparity. In addition, the total bandwidth used to generate overall sound pressure levels was 6 kHz for the experiment but was effectively infinite for the calculation. This difference could be partially responsible for the noted higher overall amplitude level of the numerical computation.

Figure 9 displays the frequency spectra of the three-dimensional computation compared with the two-dimensional result. Only a slight disparity in the predicted frequencies of the harmonics is observed, although the level of the two-dimensional solution is somewhat higher.

A simple representation of the unsteady flowfield structure is provided by Fig. 10, which indicates instantaneous cross-plane velocity vector plots within the cavity at three axial locations for $t = t_f$. The most prominent feature observed in the figure is the vortex which is seen to emanate upstream ($x/L = 0.25$) from fluid flowing inboard over the mouth of the cavity at the sidewall. Near midcavity ($x/L = 0.5$), the vortical flow is quite evident and gives rise to several regions of secondary structure. Further downstream ($x/L = 0.75$), a single large vortex completely fills the half-span cavity. It should be noted that the magnitude of the velocities within the cavity are quite small. In addition, the vectors shown in the figure are instantaneous values of an unsteady process. However, it is possible to interpret the comparisons between the two-dimensional and three-dimensional solutions on the basis of Fig. 10. Generally, it would be expected that a three-dimensional flowfield produce slightly lower pressure levels than a corresponding two-dimensional flow due to the relief effect. For the cavity, this was typically true for $x/L < 0.5$. Downstream, however, the presence of a fully developed vortical structure has degraded this behavior.

The three-dimensional nature of the cavity flowfield is also indicated in Fig. 11, which shows instantaneous axial pressure

distributions at the cavity mouth ($y/D = 1.0$) for several spanwise locations at $t = t_f$. Once again it is seen that upstream the spanwise variation is minor. Downstream, however, the presence of the vortex has produced a more significant impact on the flowfield, particularly where it interacts with the aft bulkhead.

The time history of the fluctuating centerline pressure on the rear bulkhead at $y/D = 0.6$ is displayed in Fig. 12. For comparison, the mean pressure level is also indicated. It can be observed that although the mean pressure value is only about 30% higher than freestream, peak levels can be as much as 2.8 times $p_\infty$. Also, the first harmonic of the oscillation, which is approximately 1 kHz, corresponds to the spacing between major pressure peaks of $\Delta t \approx 10^{-3}$. The broadband fluctuating pressure response displayed in Fig. 12 is characteristic of high Reynolds number viscous flows and was not observed in the solution of the Euler equations[12] that produced an extremely periodic pressure time history comprised of few frequency components.

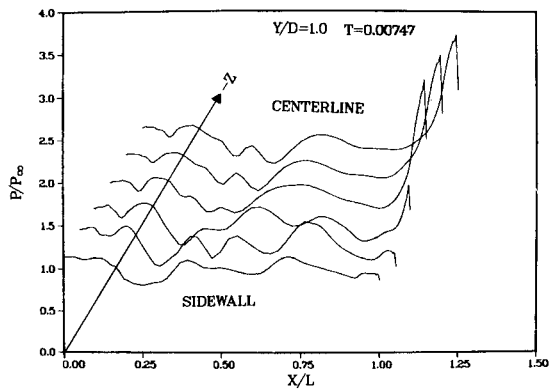


**Fig. 11 Instantaneous streamwise pressure distributions across the cavity mouth at $t = t_f$.**

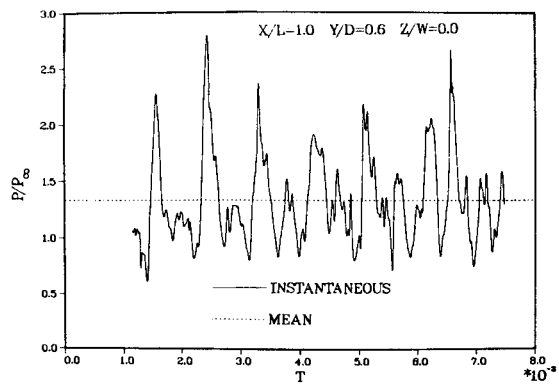


**Fig. 12 Pressure time history on the aft bulkhead at the centerline.**

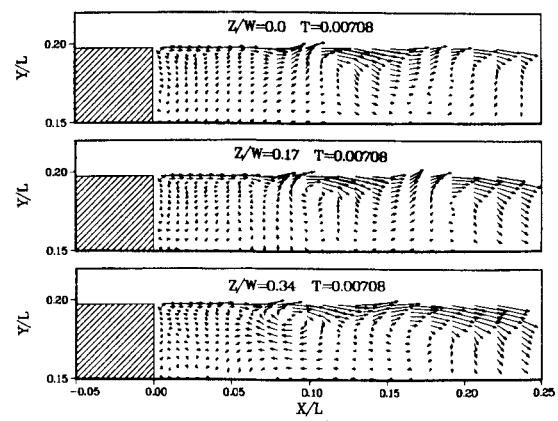


**Fig. 13 Instantaneous streamwise velocity vectors at the forward bulkhead.**

Instantaneous velocity vectors in the $x$-$y$ plane near the top of the forward bulkhead at three spanwise locations are presented in Fig. 13. The purpose of this figure is to indicate the generation of vorticity which occurs at the forward cavity lip and is convected downstream. Along the centerline ($z/W = 0$), two vortices which originated at the lip ($x = 0$) appear at $x/L = 0.11$, 0.20. At the other spanwise locations ($z/W = 0.17$, 0.34), a similar structure is observed, although the $x$ location of the vortices is different. This periodic shedding of vorticity from the lip of the forward bulkhead is observed repeatedly throughout the oscillation cycle, verifying the simple physical model envisioned by Rossiter. It should be noted, however, that the phenomenon is highly three-dimensional and more complex than the planar situation which Rossiter proposed.

Figure 14 indicates the cavity flowfield near the rear bulkhead. Instantaneous velocity vectors in the $x$-$y$ plane for three spanwise locations are shown at two different values of time. For clarity, vectors are displayed only at every other $x$-grid location. At $t = 0.00678$, the fluid near the rear bulkhead is seen to flow up over the top of the aft lip of the cavity, representing expulsion of fluid. Later in time ($t = 0.00687$), mass injection into the cavity occurs at all three spanwise stations as indicated by the downward flow near the rear bulkhead. Once again it should be mentioned that these features are three-dimensional and do not appear in a simple periodic fashion. They are, however, observed to recur frequently and must be considered fundamental to the basic mechanism of the oscillation.

The inviscid portion of the flowfield lying above the mouth of the cavity is extremely complex. Undulation of the oscillating shear layer results in a series of compression and expansion waves in the inviscid flowfield which are unsteady and three-dimensional. Figure 15 provides only a representative illustration of this behavior in terms of instantaneous static pressure contours in the plane of symmetry at two different time levels. For

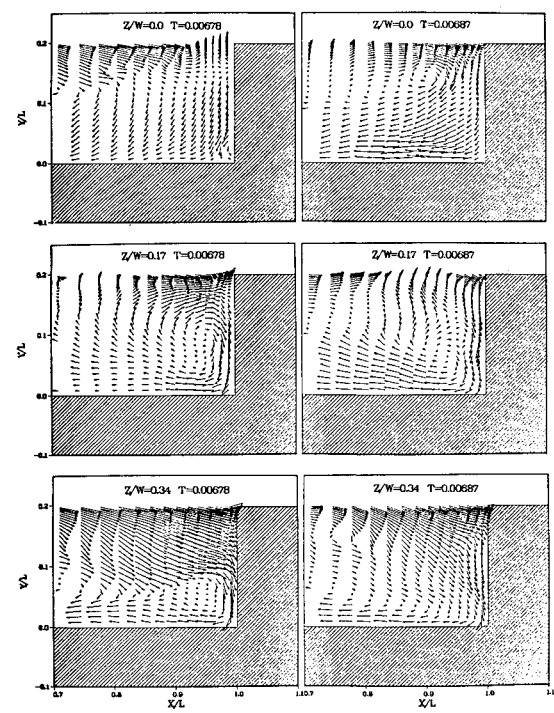


**Fig. 14 Instantaneous streamwise velocity vectors at the rear bulkhead.**

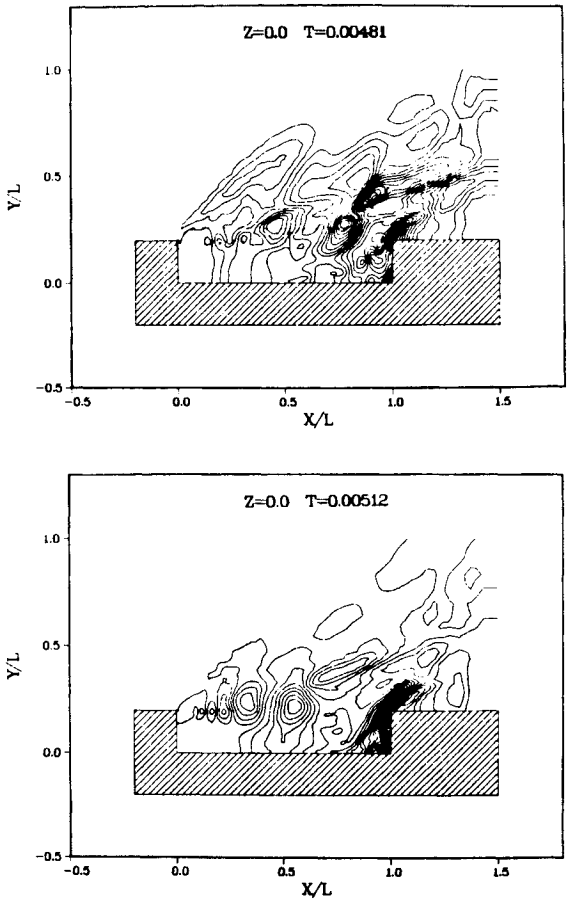


**Fig. 15 Instantaneous streamwise pressure contours at the centerline.**

$t = 0.00481$, a pressure wave above the mouth of the cavity is seen to be located at $x/L \approx 0.8$. This wave moves downstream, impacts the rear bulkhead, and begins to travel upstream as shown for $t = 0.00512$. In the upstream region of the cavity, the alternating sequence of compressions and expansions produced by the waviness of the shear layer is evident.

## Conclusions and Discussion

Although the calculation reported here was intensive in terms of computational resources, much useful information could have been obtained with the expenditure of considerably less processing time. In particular, the mean static pressure and overall sound pressure levels remained invariant after about 10,000 time steps. Moreover, the acoustic amplitudes (peak values) of harmonic frequencies also remained invariant. Additional time steps were required, however, in order to resolve the frequency spectra.

Several possibilities exist for the observed discrepancies between the numerical computation and experimental data. Among these are inadequate numerical resolution, numerical damping, and the eddy viscosity model employed. Preliminary two-dimensional investigations using approximately twice as many grid points in both the $x$ and $y$ directions indicated only a slight variation from the results presented here. Due to the unsteady nature of the problem, however, the impact of this information on the three-dimensional case is unclear. The value of the damping coefficient, $\beta$, employed for the present calculation is considered to be nominal ($\beta = 2.0$). For the two-dimensional case, a stable computation could not be produced for $\beta < 2.0$. In the three-dimensional case, no calculation with an alternate value of $\beta$ was attempted.

It is realized that the simple eddy viscosity model employed for this calculation cannot truly represent the detailed structure of the physical flow. Prior calculations have indicated[12,13] that accuracy in such detail was not crucial to the overall oscillatory behavior. Without an eddy viscosity model, however, it was found that no self-sustained oscillation was produced. The reason for this was that separation occurred upstream of the forward bulkhead if the laminar equations were solved, thus eliminating the oscillating shear layer. When the inviscid equations of motion were considered, as by Borland,[12] such separation was not an issue. The calculation of Hankey and Shang[13] produced a self-sustained unsteady flow employing the laminar Navier-Stokes equations. However, they were able to match a measured experimental velocity profile at the forward bulkhead, which was critical. In the current case, no such data was available. Thus, differences between the calculated and physical shear-layer profiles upstream of the forward bulkhead may contribute to some lack of agreement of the computation with experimental data.

A numerical solution has been presented for the unsteady flow over a three-dimensional cavity at a freestream Mach number of 1.5 and Reynolds number of $1.09 \times 10^6$. The self-sustained oscillatory flow within the cavity, which is commonly observed experimentally, has been simulated by the computation. Quantitative comparison with experimental data has been made in terms of mean static pressure, overall acoustic sound pressure level, and acoustic frequency spectra within the cavity. While most of this comparison is favorable, the numerical solution appeared to overpredict the amplitude of the harmonic frequencies. Comparison with a two-dimensional calculation verified that the fundamental behavior of the oscillation is two-dimensional. The presence of a vortex evolving at the sidewall of the forward bulkhead, however, was seen to produce a three-dimensional effect.

## Acknowledgments

Computational resources for the work presented here were provided through the auspices of the NAS Computational Facility, NASA Ames Research Center, Moffett Field, CA. The author is grateful to J. S. Shang for many useful conversations and wishes to thank R. M. Shimovetz for his help in the comparison with experimental data.

## References

[1]Krishnamurty, K., "Acoustic Radiation From Two-Dimensional Rectangular Cutouts in Aerodynamic Surfaces," NACA TN-3487, Aug. 1955.

[2]Charwat, A. F., Roos, J. N., Dewey, F. C., Jr., and Hitz, J. A., "An Investigation of Separated Flows—Part I: The Pressure Field," *Journal of the Aerospace Sciences*, Vol. 28, June 1961, pp. 457–470.

[3]Charwat, A. F., Dewey, C. F., Jr., Roos, J. N., and Hitz, J. A., "An Investigation of Separated Flows Part II: Flow in the Cavity and Heat Transfer," *Journal of the Aerospace Sciences*, Vol. 28, July 1961, pp. 513–527.

[4]Rossiter, J. E. and Kurn, A. G., "Wind Tunnel Measurements of the Unsteady Pressures In and Behind a Bomb Bay (Canberra)," Ministry of Aviation, Aeronautical Research Council, London, England, CP 728, Oct. 1962.

[5]Rossiter, J. E., "Wind Tunnel Measurements on the Flow Over Rectangular Cavities at Subsonic and Transonic Speeds," Ministry of Aviation, Aeronautical Research Council, London, England, R&M 3438, Oct. 1964.

[6]East, L. F., "Aerodynamically Induced Resonance in Rectangular Cavities," *Journal of Sound and Vibration*, Vol. 3, May 1966, pp. 227–287.

[7]Heller, H., Holmes, G., and Covert, E., "Flow Induced Pressure Oscillations in Shallow Cavities," AFFDL-TR-70-140, Dec. 1970.

[8]Bilanin, A. J. and Covert, E. E., "Estimation of Possible Excitation Frequencies for Shallow Rectangular Cavities," *AIAA Journal*, Vol. 11, March 1973, pp. 347–351.

[9]Heller, H. and Bliss, D., "Aerodynamically Induced Pressure Oscillations in Cavities: Physical Mechanisms and Suppression Concepts," AFFDL-TR-74-133, Feb. 1975.

[10]Heller, H. H. and Bliss, D. B., "The Physical Mechanism of Flow-Induced Pressure Fluctuations in Cavities and Concepts For Their Suppression," AIAA Paper 75-491, March 1975.

[11]Clark, R. L., "Weapons Bay Turbulence Reduction Techniques," AFFDL-TM-75-147, Dec. 1975.

[12]Borland, C. J., "Numerical Prediction of the Unsteady Flowfield in an Open Cavity," AIAA Paper 77-673, June 1977.

[13]Hankey, W. L. and Shang, J. S., "Analyses of Pressure Oscillations in an Open Cavity," *AIAA Journal*, Vol. 18, Aug. 1980, pp. 892–898.

[14]Clark, R. L., Kaufman, L. G. II, and Maciulaitis, A., "Aero-Acoustic Measurements for Mach 0.6 to 3.0 Flows Past Rectangular Cavities," AIAA Paper 80-0036, Jan. 1980.

[15]Kaufman, L. G. II, Maciulaitis, A., and Clark, R. L., "Mach 0.6 to 3.0 Flows Over Rectangular Cavities," AFWAL-TR-82-3112, May 1983.

[16]Baldwin, B. S. and Lomax, H., "Thin Layer Approximation and Algebraic Model for Separated Turbulent Flows," AIAA Paper 78-257, Jan. 1978.

[17]Shang, J. S. and Hankey, W. L. Jr., "Numerical Solution for Supersonic Turbulent Flow Over a Compression Ramp," *AIAA Journal*, Vol. 13, Oct. 1975, pp. 1368–1374.

[18]MacCormack, R. W., "The Effect of Viscosity in Hypervelocity Impact Cratering," AIAA Paper 69-354, April 1969.

[19]MacCormack, R. W. and Baldwin, B. S., "A Numerical Method for Solving the Navier-Stokes Equations with Application to Shock-Boundary Layer Interaction," AIAA Paper 75-1, Jan. 1975.